Surface Science 606 (2012) 670–677

Contents lists available at SciVerse ScienceDirect

Surface Science

journal homepage: www.elsevier.com/locate/susc

Preparation, surface state and band structure studies of $SrTi_{(1-x)}Fe_{(x)}O_{(3-\delta)}$ (x = 0–1) perovskite-type nano structure by X-ray and ultraviolet photoelectron spectroscopy

Mohammad Ghaffari [a,b,c,*], Mark Shannon [b], H. Hui [a], Ooi Kiang Tan [a], Ahmad Irannejad [d]

[a] School of Electrical and Electronic Engineering, Nanyang Technological University, 50 Nanyang Avenue, Singapore 639798, Singapore
[b] Mechanical Science and Engineering, University of Illinois at Urbana-Champaign, Urbana, Illinois 61801, USA
[c] Department of Electrical and Electronics Engineering, UNAM - National Institute of Materials Science and Nanotechnology, Bilkent University, Ankara 06800, Turkey
[d] Department of Materials Science and Engineering, School of Engineering, Shahid Bahonar University of Kerman, Kerman, Iran

ARTICLE INFO

Article history:
Received 29 August 2011
Accepted 19 December 2011
Available online 27 December 2011

Keywords:
$SrTi_{(1-x)}Fe_{(x)}O_{(3-\delta)}$ (STF_x)
Perovskite
High temperature solid state reaction
EXAFS
XPS
UPS

ABSTRACT

In this report, $SrTi_{(1-x)}Fe_{(x)}O_{(3-\delta)}$ photocatalyst powder was synthesized by a high temperature solid state reaction method. The morphology, crystalline structures of obtained samples, was characterized by X-ray diffraction (XRD), scanning electron microscope (SEM), and transmission electron microscopy (TEM), respectively. The electronic properties and local structure of the perovskite STF_x ($0 \le x \le 1$) systems have been probed by extended X-ray absorption fine structure (EXAFS) spectroscopy. The effects of iron doping level x (x = 0–1) on the crystal structure and chemical state of the STF_x have been investigated by X-ray photoelectron spectroscopy and the valence band edges for electronic band gaps were obtained for STF_x by ultraviolet photoelectron spectroscopy (UPS). A single cubic perovskite phase of STF_x oxide was successfully obtained at 1200 °C for 24 h by the solid state reaction method. The XPS results showed that the iron present in the STF_x perovskite structure is composed of a mixture of Fe^{3+} and Fe^{4+} ($SrTi_{(1-x)}[Fe^{3+}, Fe^{4+}]_{(x)}O_{(3-\delta)}$). When the content x of iron doping was increased, the amount of Fe^{3+} and Fe^{4+} increased significantly and the oxygen lattice decreased on the surface of STF_x oxide. The UPS data has confirmed that with more substitution of iron, the position of the valence band decreased.

1. Introduction

The perovskite-type oxides are well known among the metal oxide photocatalysts for having the important characteristics of partial substitution of the cations at both the A and B sites of ABO_3 and the ability to maintain stable mixed oxidation states or unusual oxidation states in the crystal structure. For example if the Cr (Fe) cations are alternatively doped at the Sr^{2+} site rather than the Ti^{4+} site, different photo physical and photocatalytic properties would be obtained. A wide range of cations and valences can be accommodated in this simple crystal structure due to the susceptibility of partial substitution at both the A and B sites, and so rendering perovskite to various flexible chemical tailoring [1]. As a typical ABO_3 type perovskite, $SrTiO_3$ has been known as a photocatalyst capable of decomposing H_2O into H_2 and O_2 without applying an external bias potential [2,3]. In recent years, many perovskite materials were studied, and the results of these reports on the ABO_3 that contained transition metal ions (B) presented an interesting range of electrical properties. Perovskite structure material are used in a wide range of applications such as catalysis [1,4], photocatalysis [5,6], fuel cells [7], magneto-optics [8,9], and in spin valves [10]. The stability of perovskite materials at high temperatures and in chemically aggressive atmospheres has made these materials such as $SrTiO_3$ and $BrTiO_3$ suitable as gas-sensor materials [11,12].

Strontium Titanate Ferrite, STF_x, has a continuous solid state solution between strontium ferrite, $SrFeO_3$ and strontium titanate, $SrTiO_3$. The existence of oxygen vacancies in STF_x is unavoidable because in this structure, when the iron atoms were replaced with the titanium atom and due to the difference in their preferential oxidation states (+4 for Ti and +3 for Fe), oxygen vacancies were formed in order to maintain charge balance in the system[13,14]. STF_x has found vast applications in oxygen sensor [14–16], hydrocarbon sensor [17], fuel cell [16,18], oxygen separation membranes [19] and phase shifters in communication systems [20], however the STF_x compound is yet to be fully understood and more research is needed.

This paper describes a simple procedure for the synthesis of STF_x series (x = 0~1), with x at 0.2 interval, by a high temperature solid state reaction process (1200 °C, two cycles in oxygen ambient with flow rate of 150 sccm). Next, the surface chemical states of the synthesized STF_x samples were characterized by XPS and UPS in order to elucidate the structure with a different doping of iron in the

* Corresponding author at: School of Electrical and Electronic Engineering, Nanyang Technological University, 50 Nanyang Avenue, Singapore 639798, Singapore. Tel.: +65 935 395 47.
E-mail addresses: moha0094@e.ntu.edu.sg, Mgh@illinois.edu (M. Ghaffari).

0039-6028/$ – see front matter © 2011 Elsevier B.V. All rights reserved.
doi:10.1016/j.susc.2011.12.013

$SrTiO_3$ perovskite structure. The crystal structure was examined with quantitative X-ray diffraction (XRD).

2. Experimental

Strontium carbonates ($SrCO_3$, 99.9%), iron oxide (α-Fe_2O_3, 98.9%) and titanium dioxide (anatase TiO_2, 99.9%) were commercially obtained and supplied by Aldrich. The synthesis of STF_x powders ($x = 0$, 0.2, 0.4, 0.6, 0.8 and 1) was carried out with high temperature solid state reaction technique. First, strontium carbonate, iron oxide and titanium dioxide powders were prepared according to the x value, and then mixed manually in an agate mortar for 15 min. The mixture was calcinated at 1200 °C for 24 h in oxygen ambient, with a flow rate of 150 sccm. Next, furnace cooled to room temperature down and grinded again manually in the agate mortar for 15 min. The ground powder was further calcinated at 1200 °C for another 24 h and furnace cooled to room temperature in oxygen ambient.

The phase structure of the powders was identified using a Shimadzu Laboratory XRD-6000 instrument. Powder XRD patterns were collected over the angular range of 20–80° 2theta using Bragg–Brentano geometry (Cu Kα source, primary and secondary Soller slits, 0.1 mm divergence slits, 0.3 mm receiving slit and secondary graphite monochromator). The diffractometer was calibrated using a laboratory standard (NIST SRM 660a). The surface chemical composition of the powders was monitored by X-ray Photoelectron spectroscopy (XPS) measurements, performed with a Kratos Axis ULTRA X-ray Photoelectron Spectrometer and an Mg Kα anode (1253.6 eV photon energy, 15 kV, 300 W) at a take-off angle of 45°. Valence band UPS experiments were performed using He *I* (21.22) eV and Al Kα (1486.6) eV photon lines. Binding energies were calibrated by measuring the Fermi step position and the Au $4f_{7/2}$ core level of a clean gold film.

3. Results and discussion

3.1. Structure and microstructure analysis

The XRD analysis was performed for STF_x powders for x varying from 0 to 1 and shown in Fig. 1(a). All peaks were indexed, indicating that Fe is dissolved within the crystal lattice of the $SrTiO_3$ compound. All the diffraction peaks can be indexed by standard card number of 91062-ICSD, indicating the continuous solid solution of Fe in $SrTiO_3$. The XRD peaks shift to a higher diffraction angle with increasing Fe concentrations, which is evidence for the increasing substitutional doping of Fe in STF_x (Fig. 1(b)). The ionic radius of Fe^{3+} (0.585) is smaller than Ti^{4+} (0.605), hence doping of Fe leads to a decreased lattice parameters and interplanar spacing in STF [21] .

The Rietveld refinements of the XRD data were carried out using the perovskite structure (space group: $PM\bar{3}M$) and the 91062-ICSD standard card number to measure the crystallite size, lattice parameter, strain and oxygen vacancy. Rietveld analysis is a semi-quantitative method of analyzing the whole diffraction pattern of X-ray or neutron powder diffraction. For extracting more precise information, a single-number integrated intensity I_{obs} is replaced (i.e. spread out) by a peak with heights y_i along the points of a step scan in 2-theta [22]. Fig. 2 shows the Rietveld pattern determined from X-ray powder diffraction data for $SrFeO_3$. Plots denote observed data, the red line denotes calculated profiles, and the green line denotes the difference. The vertical lines indicate possible Bragg peaks of the monoclinic $SrFeO_3$ phase. Table 1 shows the values of the crystallite size, lattice parameter, oxygen vacancy, lattice strain and R-Bragg of STF_x compositions obtained with Rietveld refinement. The doping of Fe can induce a high tendency of oxidization. Thus, the crystallites size increases as well. Moreover, the lattice parameter of the samples due to difference of the ionic radius of the Fe and Ti, decrease from 3.9083 (Å) to 3.8601 (Å). oxygen vacancy (δ) is a result of charge neutrality. The oxygen vacancy (δ) must decrease with increasing doping content of Fe to maintain the charge neutrality of the compound. This is also confirmed by XPS analysis that will be explained later. The local lattice strain shows a fluctuation that can be explained by increasing the distortion and mismatch of the structure with Fe doping.

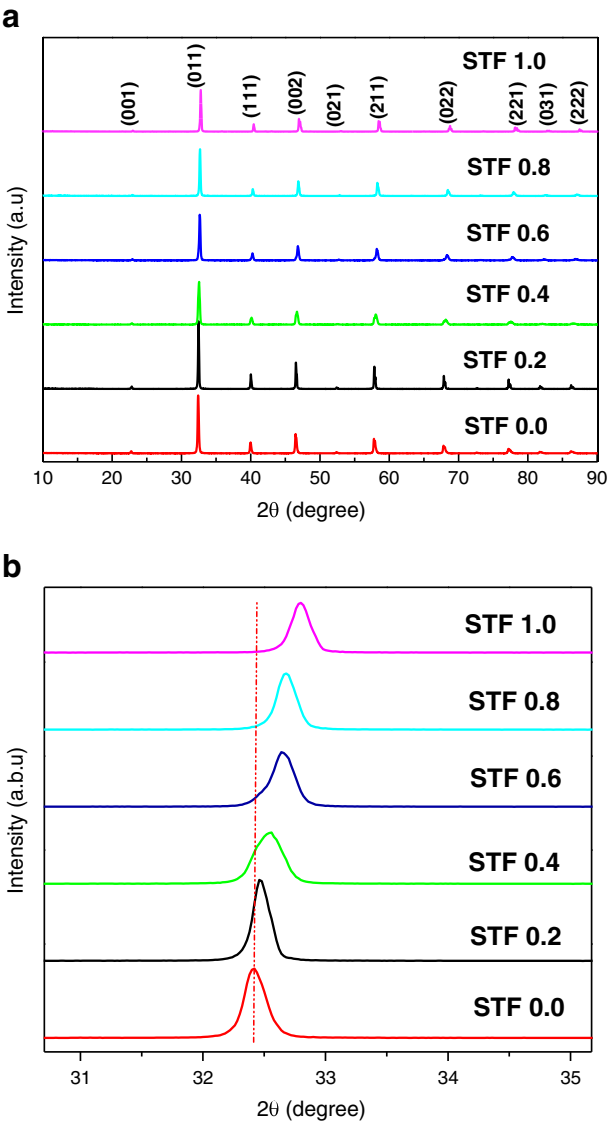

Fig. 1. (a) XRD patterns of STF_x at different x; (b) shift of (011) peaks.

Fig. 3(a), (b) shows the TEM and SEM images of $SrFeO_3$ (SFO) particles respectively. Selected area electron diffraction (SAED) patterns confirm the strontium ferrite crystallite (Fig. 3(a)). Fig. 3(a) present the indexing of $SrFeO_3$ (SFO) powder with [111] zone axis.

3.2. XAFS study

The coordination chemistry of iron (titanium) was of particular interest. Information about the pre-edge features of the X-ray absorption near the edge structure (XANES) region was related to the d-electron configuration and local symmetry of iron (titanium). The extended X-ray absorption fine structure (EXAFS) region was used to probe local geometric structures up to several coordination shells around iron (titanium) ions, where the Fe–O (Ti–O) distance was of interest in connection with the valence state of iron. The Fe and Ti K-edge XANES spectra for the STF_x samples at various x (0, 0.2, 0.4, 0.6, 0.8 and 1) are shown in Fig. 4(a) and (b), the standard Fe and Ti foils are also presented. Fig. 5 shows a schematic representation

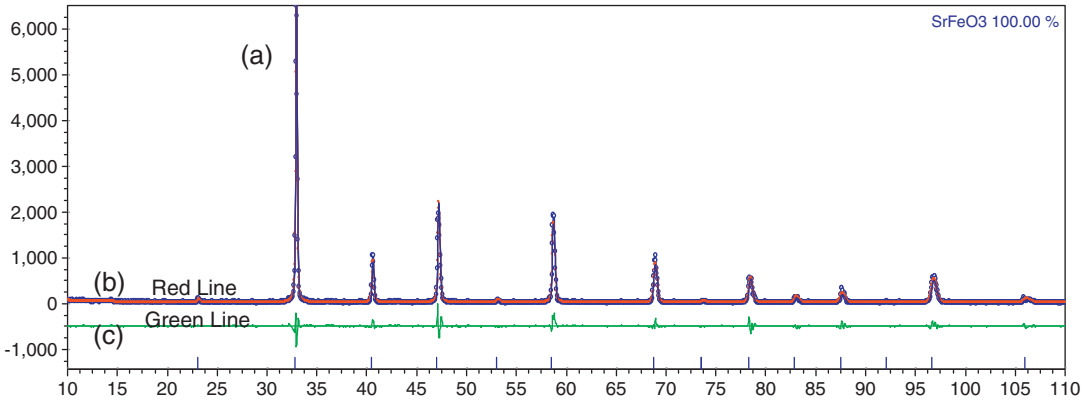

Fig. 2. Rietveld pattern determined from X-ray powder diffraction data for $SrFeO_3$.

of the atomic orbitals for Fe^{+3} and Fe^{+4} and the expected K-edge XAS transitions to half occupied or empty orbitals and into the continuum. In an octahedral crystal field, the t_{2g} orbitals occur at lower energy than the e_g orbitals. This is a reflection of the orientation of the orbitals since the t_{2g} are directed between bond axes while the e_g point along bond axes. The Jahn–Teller Theorem predicts that distortions should occur for any degenerate state, including degeneracy of the t_{2g} level, however distortions in bond lengths are much more distinctive when the degenerate electrons are in the e $_g$level [23,24].

At the K-edge X-ray excitation, electrons of 1s orbitals are transferred to partially occupied or empty states (XANES region) nearby the Fermi level (3d and 4p-related orbitals), at higher energy X-rays electrons jump to the continuum (EXAFS region, where the outgoing electrons are scattered by neighboring atoms) [25–27]. Structural data on cubic perovskite AB_3 (A = Sr, B = Ti, Fe) suggests that 6 oxygen atoms are observed in the cation first coordination sphere in position B. The second and third coordination spheres contain 8 strontium atoms and 6 metal atoms, respectively [28]. The pre-edge peaks A and B, main peaks C and D in Fig. 4(a) can be identified.

The pre-edge peaks were related to a pure quadrupole origin due to $1s \rightarrow 3d$ transitions in transitional metal oxides [29–31]. Under careful observation, the peak A for $SrTiO_3$ appears to be actually made of two peaks. As reported earlier [32,33], A_1 is a pure quadrupolar (E2), A_2 is partial quadrupolar (and partial dipolar), B is pure dipolar (E1). Even in $SrTiO_3$, a high distortion in TiO_6 was observed. A is lowest for the perfect octahedral TiO_6 (Oh symmetry) and can be enhanced by a distortion to Oh due to the loss of centro-symmetry. It was suggested that the intensity of the peak B is proportional to a displacement of Ti atoms from the center of the TiO_6 octahedra [30] but inversely related to the Ti–O bond length. The peak C is a 4p-related "shape resonance" in the continuum part of the spectrum and the peak D is attributed to more delocalized states [34,35]. The XANES spectra show almost no edge shift as a function of x but its intensity and shape change systematically with x.

Table 1
Crystallite size, lattice parameter, oxygen vacancy, lattice strain and R-Bragg values of STF_x powders calculated from Rietveld refinement.

x in STF_x	Crystallite size (nm)	Lattice parameter (Å)	Oxygen vacancy (δ)	Lattice strain (%)
0	243.6	3.908	0.0207	0.0116 (L)*
0.2	280.4	3.901	0.0735	0.3519 (L)*
0.4	320.2	3.894	0.1554	0.6372 (L)*
0.6	350.5	3.884	0.2067	0.4981 (L)*
0.8	378.3	3.874	0.2466	0.2377 (L)*
1	445.8	3.860	0.2566	0.3348 (L)*

*Strain L means Lorentzian (This described the symmetrical part of an X-ray diffraction peak).

The spectra with low Fe content exhibit the lowest pre-edge peak A intensities in Fig. 4(a), with increasing Fe contents. Peak A is stronger and not resolved into two peaks, while peak B shifts slightly to high energy. The peak C also slightly shifts toward high energy. Within the accuracy limit of XANES, any changes or splitting with the peak A in Fig. 4(b) is not observable. This may be due to the more closely

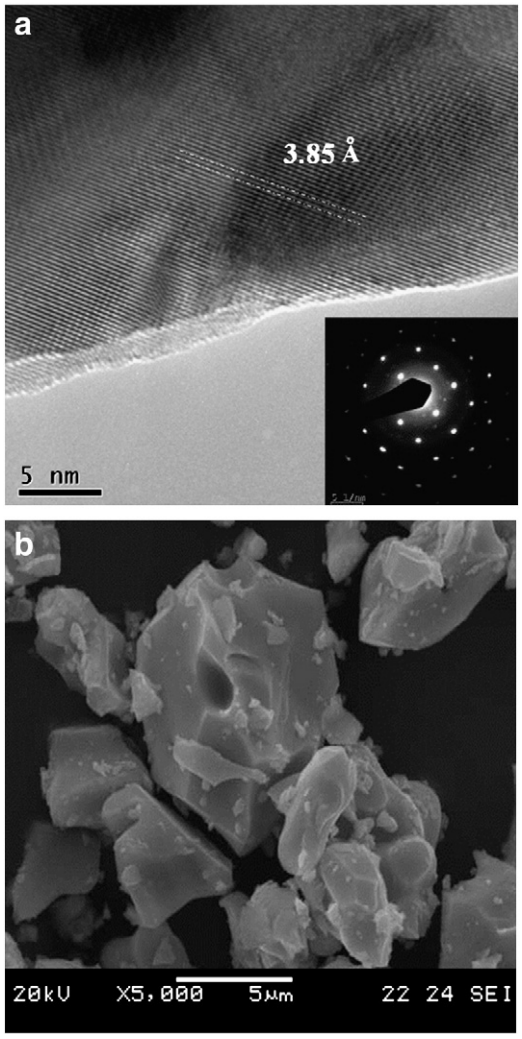

Fig. 3. (a) TEM micrographs of $SrFeO_{(3-\delta)}$ and SAED patterns could be indexed as strontium ferrite with [111] zone axis and (b) SEM micrograph of the strontium ferrite particles at 1200 °C temperatures × 10,000.

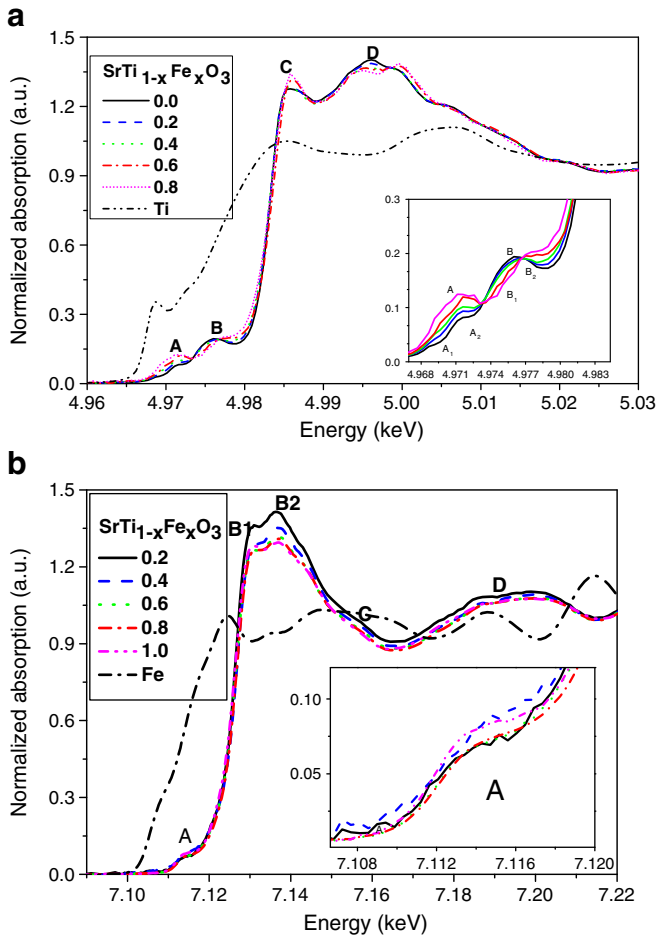

Fig. 4. Ti K-edge (a) and Fe K-edge (b) XANES spectra of the $SrFe_xTi_{(1-x)}O_3$ samples at x = 0, 0.2, 0.4, 0.6, 0.8, 1. The inset in (a) is pre-edge peaks for Ti K-edge and (b) Fe K-edge.

packed FeO_6 clusters and highly symmetry because of the smaller atomic radius for Fe. With increasing Fe dopant, the intensities of B_1 and B_2 and their ratios change continuously. No significant shift for the main peak was observed in Fig. 4(b).

3.3. XPS studies

The surface composition of the STF_x series samples was characterized by XPS technique. All XPS spectral peaks were fitted with CASAXPS software. The data analysis involved spectra normalization, Shirley background subtraction, and curve-fitting Gaussian–Lorentzian (30% Lorentzian) line shapes [36]. Best fits were evaluated using a root-mean-square measure where line shape, peak width (full width at half maximum, or FWHM) and binding energy were adjustable parameters. Shirley backgrounds were used in all fits to narrow scan spectra [37]. As required by theory, O 1s and C 1s spectral lines consist of a single peak (a singlet) whereas the Fe 2p, Ti 2p and Sr 3d spectrum consist of two peaks, a spin-orbit doublet. The C 1s spectral line was standardized to 285.0 eV and the O 1s, Fe 2p, Ti 2p and Sr 3d spectra were adjusted to this energy.

To illustrate the spectral features of the STF_x series samples, the O 1s, C 1s, Sr 3d, Fe2p and Ti 2p peaks are summarized in Figs. 6 and 7, respectively. Deconvolution of the O 1s spectra yields three peaks, namely O 1s a (529.0 eV), O 1s b (531.2 eV) and O 1s c (532.9 eV). From the literature, the peak at the 532.9 eV is probably due to the water and hydroxide absorbed on the surface [38–41], while the peaks at 531.2 eV correspond to carbonate compounds and chemical Adsorption [42–51]. The main peaks at 529.0 eV (O 1s a) correspond to the oxygen lattice [19,20,50]. Quantitative analysis has shown that with increasing iron content in STF_x series, the amount of the oxygen lattice decreases. This observation can be attributed to the partial substitution of Fe with Ti, iron participation with mixed oxidation state of Fe^{3+} to Fe^{4+} and the formation of oxygen vacancy that consequently led to the reduction of the amount of oxygen lattice. The ratio of O 1s a is presented in Table 2, shows that with increasing iron content this ratio decreased. This can be explained by the formation of the oxygen vacancy with Fe occupying the Ti site. Fig. 6(b) shows the detailed peak scan for C 1s. Three peaks were observed, namely C 1s a (285 eV), C 1s b (286.1 eV) and C 1s c (289.1 eV). The low binding energy peak at 285 eV with strong intensity is the result of the presence

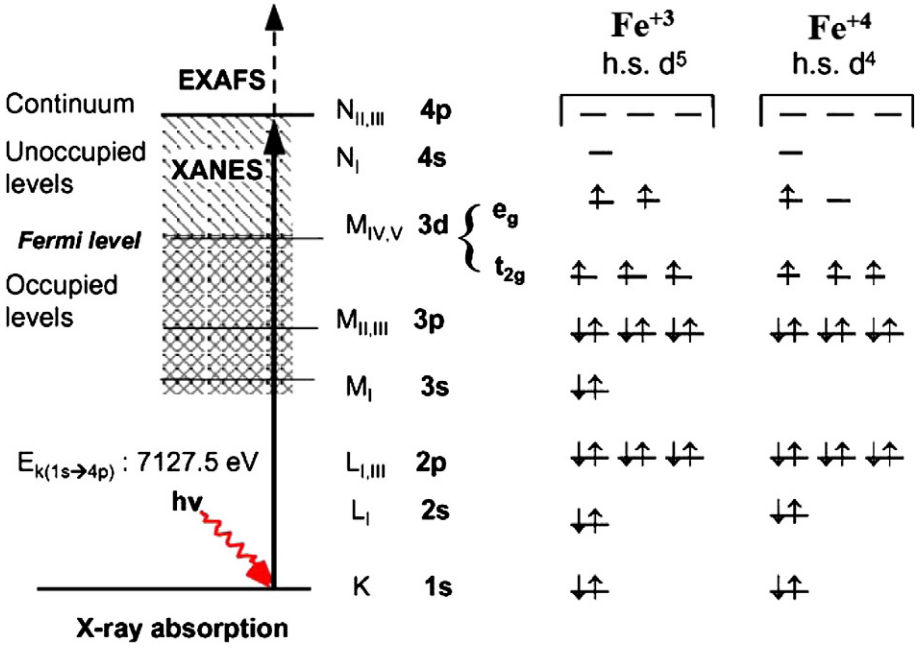

Fig. 5. Molecular orbital scheme of Fe^{+3} and Fe^{+4} with possible XAS transitions.

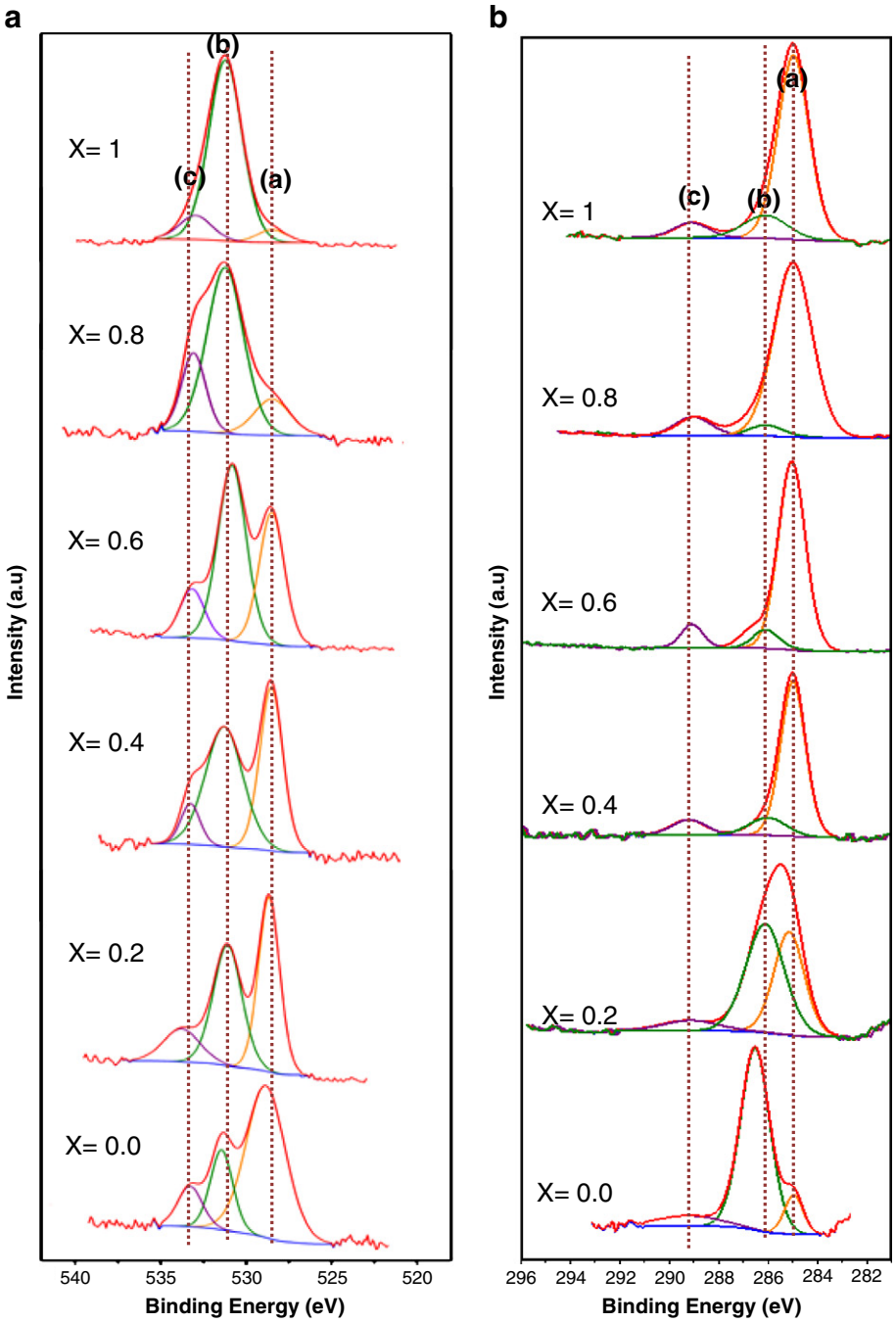

Fig. 6. The core level XPS spectra for STF for x = 0 ~ 1 for (a) O 1s, (b) C 1s.

of adventitious carbon (C–H) [44,45,50], which is due to atmospheric contamination and is always present on a solid surface that is used as the calibration reference. The higher binding energy at 286.1 eV is possibly due to the CO like species (C–O) [44]. The well-defined peak at 289.1 eV is related to carbonates (O–C–O and/or C = O) [42,50,52] as a result of the perovskite thermal treatment.

The Sr 3d spectrum can be fitted with three spin-orbital doublet pairs that originate from different chemical coordination of Sr, namely Sr 3d (a), Sr 3d (b) and Sr 3d (c). The Sr 3d regions were fitted by doublets with fixed spectroscopic parameters, spin-orbital separation (1.8 eV) and $3d_{3/2}$:$3d_{5/2}$ branching ratio of 0.667, but with independent and variable full width half maximum (fwhm), positions and intensities, as optimized by the fitting program. The Sr $3d_{3/2}$ and $3d_{5/2}$ spectrum presents two doublets. The first is at binding energies 132.6 and 130.8, the second at 133.7 eV and 131.9 eV, and the third at 135.6 eV and 133.8 eV (Fig. 7(a)). The main doublet feature centered at ~133.8 eV is the characteristic of perovskite crystal, while the other features shift toward lower energy by ~1.8 eV can be attributed to to $SrCO_3$ and the peak. The peak of Sr 3d (a) at 130.8 eV was observed only for STF_1 which can be attributed to the Sr ions surrounded by vacancies in the oxygen-deficient perovskite structure that is similar to that of $SrO_{(1-x)}$. This phenomenon can be explained by the dramatic increase of Fe^{3+} and Fe^{4+} in $SrTi_{(1-x)}[Fe^{3+}, Fe^{4+}]_{(x)}O_{(3-\delta)}$ perovskite structure [45,53,54]. The peaks at 131.9 eV Sr 3d (b) observed for all samples correspond to $SrCO_3$ and the peak at 133.80 eV, Sr 3d (c) observed corresponds to Sr (Perovskite) respectively (Fig. 6(a)) [26–28,34]. The Sr/Fe ratio is higher by more than 3-fold than the stoichiometric Sr/Fe = 1 value for STF_0, and it decreases slightly with

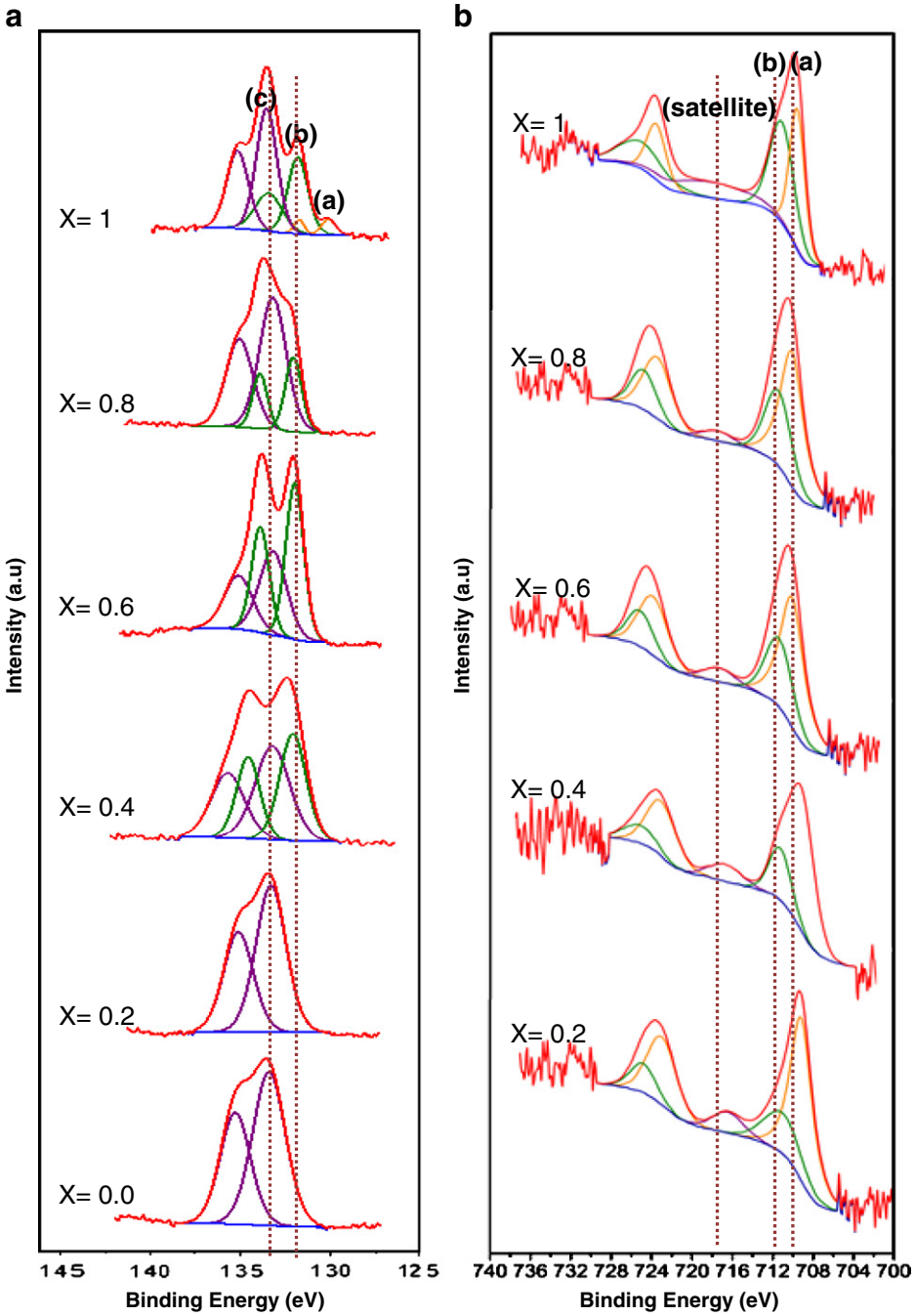

Fig. 7. The core level XPS spectra for STF for x = 0 ~ 1 for (a) Sr 3d and (b) Fe 2p.

decreasing O content of the STF_x perovskite. This result indicates that Sr is segregated toward the surface of the samples. It was found that a Gaussian–Lorentzian (GL) ratio of 30 in the fitting parameters give the best goodness of fit, $\chi 2$ is close to 1. Moreover in Strantium peak fitting we can assign Sr(a) peak that only for STF_1 and if added any other third peak the Sr(a) and Sr (b) overlapping in the same position.

The nature of the iron species in the STF samples can be determined by deconvoluting the XPS spectra of the Fe 2p spectral regions (Fig. 7(b)). In all the cases it can be observed the presence of a main band centered at 710.1 eV accompanied by a secondary one displaced 13.7 eV to higher binding energy (723.8 eV), in addition to a satellite peak around 719.9 eV confirming the presence of Fe^{3+} species in the surface of all STF samples [55–58].

The Fe 2p XPS region (Fig. 7(b)) shows a doublet of 2p3/2 and 2p1/2. By deconvoluting the Fe 2p spectra, two components can be obtained. The Gaussian fitting of the peaks into the component of Fe^{3+} and Fe^{4+} is also indicated in Fig. 7(b). The peaks at 710.0 eV (Fe 2p (a)) and 723.9 eV are similar to those reported for Fe 2p study and the shake-up contribution at about 719.9 eV is consistent with the presence of Fe^{3+}. The second doublet peaks appeared at 711.9 eV (Fe 2p (b)) and 725.6 eV could be assigned to Fe^{4+}.

The fitting results and the ratio of Fe^{3+} and Fe^{4+} are presented in Table 2. It was obvious that iron in STF_x perovskite structure participated in the mixture of Fe^{3+} and Fe^{4+} ($SrTi_{(1-x)}[Fe^{3+}, Fe^{4+}]_{(x)}O_{(3-\delta)}$) and with increasing iron dopant the amount of Fe^{3+} and Fe^{4+} increased significantly. Bocquet et al. investigated the electronic structure of the Fe^{4+} perovskite oxide $SrFeO_3$ by XPS, and concluded that the large increase in charge at the Fe site led to a chemical shift to a higher binding energy [56,58,59]. Moreover with an increasing amount of Fe^{4+}, the shape of the satellite also changed. P. Mills et al. [41] and

Table 2
Atomic concentrations calculated from XPS results for STF powders with x = 0~1.

Elements	Sample	Atomic concentrations (%) for $SrTi_{(1-x)}Fe_{(x)}O_{(3-\delta)}$ @ different x					
		x = 0	x = 0.2	x = 0.4	x = 0.6	x = 0.8	x = 1
	Binding energy (eV)						
Fe 2p a (Fe^{3+})	710.1	0	1.34	1.96	3.46	5.02	5.36
Fe 2p b (Fe^{4+})	711.8	0	0.47	0.79	1.69	3.87	4.19
Fe Satt	718.2	0	0.249	0.14	0.27	0.19	0.33
O 1s a	529	20.61	11.3	9.8	5.15	2.82	1.62
O 1s b	531.2	12.45	18.3	19.23	20.16	20.85	23.74
O 1s c	532.9	1.4	2.1	1.83	2.15	2.83	1.6
Ti 2p (Ti^{4+})	457.3	5.31	5.42	5.03	3.7	2.24	0
C 1s a	285	14.85	29.45	37.1	36.7	38.9	40.03
C 1s b	286.1	29.96	18.74	5.7	10.69	4.8	5.8
C 1s c	289.1	1.79	2.22	5	3.45	5.07	3.9
Sr 3d a	130.8	0	0	0	0	0	0.58
Sr 3d b	131.9	0	0	7.44	7	5.03	5.6
Sr 3d c	133.8	13.7	10.48	6.04	5.58	8.39	7.26
Total	-	100.0	100.0	100.07	100.0	100.0	100.0
Elements	Ratio						
Ti/Fe	-	0	2.65	1.75	0.67	0.25	0
Fe^{+3}/Fe^{+4}	-	0	2.83	2.48	2.05	1.31	1.28

other researchers [42] presented that the position of the satellite state is the key and finger print to detect the oxidation state of Fe. The surface oxidation can also be changed by increasing the oxidation state. For α-Fe_2O_3, the shake-up satellite peaks located at around 718.2 eV were approximately 8 eV higher than that of Fe 2p3/2 peak, whereas the satellite peak for FeO was approximately 6 eV from Fe $2p_{3/2}$ peak. There is no satellite peak observed for Fe_3O_4 [56,58].

A. E. Bocquet et al. [39] used a *p-d* charge-transfer cluster-model calculation to interpret the Fe 2p core levels. They defined the charge transfer energy Δ_{eff} with respect to the lowest multiplet levels of the d^4 and d^5L configurations and showed that the charge transfer energy Δ_{eff} is negative. They presented that the shape of the satellite can be used to detect the oxidation state of Fe. For the Fe 2p core-levels XPS spectra, strong satellite features were observed for the d^5 compounds with an apparently weaker satellite present for $SrFeO_3$. Similarly, the spectrum for $SrFeO_3$ was primarily composed of main peaks due to the screened $\underline{c}d^5\underline{L}$ states and satellite structure from mixed $\underline{c}d^4$ and $\underline{c}d^6\underline{L}^2$ states[59].

The XPS spectra of Ti 2p was also deconvoluted with a pair of peaks at 457.3 eV and 462.8 eV that attributed to Ti 2p 3/2 and Ti 2p 1/2 respectively and they are separated from each other by 5.7 eV. The XPS studies have also shown that titanium was involved in this compound as (+4) oxidation state.

3.4. UPS studies

Valence band UPS and core level XPS experiments were performed using He *I* (21.22) eV and Al Kα (1486.6) eV photon lines. Binding energies were calibrated by measuring the Fermi step position and the Au 4f 7/2 core level of a clean gold film. The determination of the position of the valence band (E_{VB}) from the UPS data was done by using the intersection of the linear extrapolation of the leading edge of the E_{VB} spectrum with the base line. The relationship between the energy levels (E_{VB}, E_F, and E_{vac}) and the UPS spectrum of STF_x and Au are shown in Fig. 8. The figure shows the scale of binding energy with the Fermi level of Au set at 0 V. The vacuum level (E_{vac}) should be located at 21.22 eV above the cutoff energy of the spectrum. The work functions of Au based on this definition were estimated to be 5.1 eV, respectively. According to the UPS spectrum, the value of the valence band maximum (E_{VB}) is located at 3.19 eV, 2.91 eV, 2.79 eV, 2.39 eV, 1.84 eV below the Fermi level (E_B) (0 eV) for x = 0, 0.2, 0.6, 0.8 and 1 respectively, determined by fitting a straight line into the leading edge. The secondary electron onset

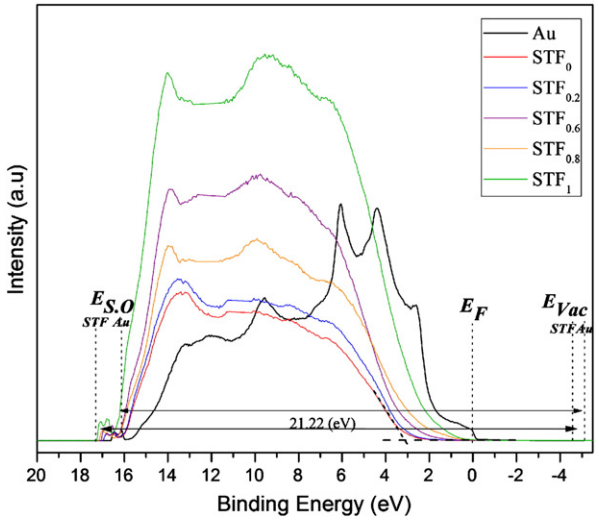

Fig. 8. Ultraviolet photoelectron spectra (He *I*) for the surface of $SrTi_{(1-x)}Fe_{(x)}O_{(3-\delta)}$.

(SO) on the left side of the spectra was measured between 16.4, 16.9 eV, and 17.2 eV for Au, STO and SFO respectively. The work function of $SrTiO_3$ was calculated to be 4.32 (±0.1) eV by subtracting the secondary electron onset position of the He *I* UPS spectra from the excitation energy (21.2 eV) [60–65].

A. Rothschild et.al [65,66] reported that with increasing Fe dopant the UPS spectra, in the range of low binding energies (<25 eV), showed that the valence band of STF_x is broader than that for $SrTiO_3$ and extended closer to the conduction band edge, which corresponded to the reduction in the band-gap energy of these compositions [65,66]. Table 3 presents the analyzed data and results of UPS measurement.

4. Conclusions

The $SrTi_{(1-x)}Fe_{(x)}O_{(3-\delta)}$ (STF_x) powders for photo catalyst application have been prepared by the high temperature solid state process. The XRD pattern indicated that a single cubic perovskite phase of STF_x powders with x varying from 0 to 1 was successfully synthesized after calcination at 1200 °C for 24 h. The lattice parameter of STF_x calculated from XRD, were in the range of 3.8601 (Å) for $STF_{x=0}$ and 3.9083 (Å) for $STF_{x=1}$. The local electronic structure of $SrFe_xTi_{(1-x)}O_3$ ($0 \le x \le 1.0$) investigated by XANES showed a dependence on composition as well as on iron oxidation state. The pre-edge features of the X-ray absorption near edge structure (XANES) region and local symmetry of iron (titanium) was successfully studied. XPS results showed that Sr ions were in 2+ oxidation state and the existence of $SrCO_3$ on the surface of samples in addition to $SrO_{(1-x)}$ on the surface of $STF_{x=1}$ was observed. Moreover, the analysis showed that iron in STF_x perovskite structure participated as a mixture of Fe^{3+} and Fe^{4+} ($SrTi_{(1-x)}[Fe^{3+}, Fe^{4+}]_{(x)}O_{(3-\delta)}$). With increasing Fe content, the amount of Fe3+ and Fe4+ increases significantly resulting in the formation of the oxygen vacancy. Consequently, with increasing oxygen vacancy, the amount of oxygen lattice would reduce. The valence

Table 3
The analyzed data and results of UPS measurement.

x in STF_x	E_{VB} [with respect to Fermi level] (eV)	E_{SO} (eV)	E_{Vac} (eV)	E_{VB} [with respect to E_{vac}] (eV)
0	3.19	16.4	−4.8	−7.79
0.2	2.91	16.48	−4.7	−7.63
0.6	2.79	16.71	−4.5	−7.28
0.8	2.39	16.8	−4.4	−6.79
1	1.84	16.9	−4.3	−6.14

band positions of STF were determined by UPS. The value of $SrTiO_3$ valence band position (E_{VB}) was reasonably consistent with the results of previous reported works. Moreover, the change in the band positions of UPS analysis was in good agreement with the modeling data reported by A. Rothschild and et.al [65,66]. UPS results further showed that the Fermi level in the Fe-doped samples was located at 4.82 ($\pm$0.1) (for $STF_{x=1}$)–4.32 ($\pm$0.1) (for $STF_{x=0}$) eV which is below the E_{Vac}.

References

[1] M.A. Peña, J.L.G. Fierro, Chem. Rev. 101 (2001) 1981.
[2] L. Tejuca, J. Fierro, Properties and Applications of Perovskite-type Oxides, CRC, 1993.
[3] M.S. Wrighton, A.B. Ellis, P.T. Wolczanski, D.L. Morse, H.B. Abrahamson, D.S. Ginley, J. Am. Chem. Soc. 98 (1976) 2774.
[4] J. Fernandes, D. Melo, L. Zinner, C. Salustiano, Z. Silva, A. Martinelli, M. Cerqueira, C. Alves Junior, E. Longo, M. Bernardi, Mater. Lett. 53 (2002) 122.
[5] X. Niu, H. Li, G. Liu, J. Mol. Catal. A: Chem. 232 (2005) 89.
[6] M. Ghaffari, P.Y. Tan, M.E. Oruc, O.K. Tan, M.S. Tse, M. Shannon, Catal. Today 161 (2011) 70.
[7] N. Minh, Solid State Ionics 174 (2004) 271.
[8] N. Keller, J. Mistrík, S. Visnovský, D. Schmool, Y. Dumont, P. Renaudin, M. Guyot, R. Krishnan, Eur. Phys. J. B 21 (2001) 67.
[9] N. Kojima, K. Tsushima, Low Temp. Phys. 28 (2002) 480.
[10] H. Sakakima, M. Satomi, E. Hirota, H. Adachi, IEEE Trans. Magn. 35 (2002) 2958.
[11] C. Alcock, R. Doshi, Y. Shen, Solid State Ionics 51 (1992) 281.
[12] R. Eglitis, S. Piskunov, E. Heifets, E. Kotomin, G. Borstel, Ceram. Int. 30 (2004) 1989.
[13] L.H. Brixner, Mater. Res. Bull. 3 (1968) 299.
[14] K. Sahner, D. Schonauer, R. Moos, M. Matam, M. Post, J. Mater. Sci. 41 (2010).
[15] W. Menesklou, H.-J. Schreiner, K.H. Härdtl, E. Ivers-Tiffée, Sens. Actuators, B 59 (1999) 184.
[16] S. Steinsvik, R. Bugge, J.O.N. GjØNnes, J. TaftØ, T. Norby, J. Phys. Chem. Solids 58 (1997) 969.
[17] K. Sahner, R. Moos, M. Matam, J.J. Tunney, M. Post, Sens. Actuators, B 108 (2005) 102.
[18] S.J. Skinner, J.A. Kilner, Mater. Today 6 (2003) 30.
[19] J.R. Jurado, F.M. Figueiredo, B. Gharbage, J.R. Frade, Solid State Ionics 118 (1999) 89.
[20] V. Varadan, D. Ghodgaonkar, V. Varadan, J. Kelly, P. Glikerdas, Microw. J. 35 (1992) 116.
[21] A. Verma, A. Kumar, S. Bhardwaj, Phys. Status Solidi B 245 (2008) 1520.
[22] L.B. McCusker, R.B. Von Dreele, D.E. Cox, D. Louer, P. Scardi, J. Appl. Crystallogr. 32 (1999) 36.
[23] I. Bersuker, I.B. Bersuker, The Jahn–Teller Effect, Cambridge Univ Pr, 2006.
[24] A. Millis, B.I. Shraiman, R. Mueller, Phys. Rev. Lett. 77 (1996) 175.
[25] M. Abbate, F. De Groot, J. Fuggle, A. Fujimori, O. Strebel, F. Lopez, M. Domke, G. Kaindl, G. Sawatzky, M. Takano, Phys. Rev. B 46 (1992) 4511.
[26] O. Haas, F. Holzer, S. Müller, J. McBreen, X. Yang, X. Sun, M. Balasubramanian, Electrochim. Acta 47 (2002) 3211.
[27] I.R. Shein, V.L. Kozhevnikov, A.L. Ivanovskii, J. Phys. Chem. Solids 67 (2006) 1436.
[28] V. Kriventsov, D. Kochubey, Z. Ismagilov, O. Podyacheva, A. Nemudry, Phys. Scr. 2005 (2005) 740.
[29] Y. Joly, D. Cabaret, H. Renevier, C. Natoli, Phys. Rev. Lett. 82 (1999) 2398.
[30] R. Vedrinskii, V. Kraizman, A. Novakovich, P. Demekhin, S. Urazhdin, J. Phys. Condens. Matter 10 (1998) 9561.
[31] T. Yamamoto, T. Mizoguchi, I. Tanaka, Phys. Rev. B 71 (2005) 245113.
[32] D. Cabaret, B. Couzinet, A. Flank, J. Itie, P. Lagarde, A. Polian, XAFS 13 (882) (2007) 120.
[33] M. Vracar, A. Kuzmin, R. Merkle, J. Purans, E. Kotomin, J. Maier, O. Mathon, Phys. Rev. B: Condens. Matter 76 (2007) 174107-174107.
[34] M. Belli, A. Scafati, Solid State Commun. 35 (1980) 355.
[35] F. Bridges, C.H. Booth, M. Anderson, G.H. Kwei, J.J. Neumeier, J. Snyder, J. Mitchell, J.S. Gardner, E. Brosha, Phys. Rev. B 63 (2001) 214405.
[36] V.P. Zakaznova-Herzog, H.W. Nesbitt, G.M. Bancroft, J.S. Tse, Surf. Sci. 600 (2006) 3175.
[37] D.A. Shirley, Phys. Rev. B 5 (1972) 4709.
[38] D. Briggs, M. Seah, Practical surface analysis by Auger and X-ray photoelectron spectroscopy, in: D. Briggs, M.P. Seah (Eds.), John Wiley & Sons, Chichester, 1983, xiv+ 533 (1983).
[39] B. Löchel, H. Strehblow, M. Sakashita, J. Electrochem. Soc. 131 (1984) 522.
[40] C. Wagner, D. Zatko, R. Raymond, Anal. Chem. 52 (1980) 1445.
[41] Q. Wu, M. Liu, W. Jaegermann, Mater. Lett. 59 (2005) 1480.
[42] N. Batis, P. Delichere, H. Batis, Appl. Catal. Gen. 282 (2005) 173.
[43] D. Fino, N. Russo, E. Cauda, G. Saracco, V. Specchia, Catal. Today 114 (2006) 31.
[44] S.M. Lima, J.M. Assaf, M.A. Peña, J.L.G. Fierro, Appl. Catal. Gen. 311 (2006) 94.
[45] B. Liu, Y. Zhang, L. Tang, Int. J. Hydrogen Energy 34 (2009) 435.
[46] N. Merino, B. Barbero, P. Eloy, L. Cadús, Appl. Surf. Sci. 253 (2006) 1489.
[47] S. Petrovic, L. Karanovic, P. Stefanov, M. Zdujic, A. Terlecki-Baricevic, Appl. Catal., B 58 (2005) 133.
[48] M. Sosulnikov, Y. Teterin, J. Electron Spectrosc. Relat. Phenom. 59 (1992) 111.
[49] R. Vasquez, J. Electron Spectrosc. Relat. Phenom. 56 (1991) 217.
[50] A. Yan, V. Maragou, A. Arico, M. Cheng, P. Tsiakaras, Appl. Catal., B 76 (2007) 320.
[51] V. Young, T. Otagawa, Appl. Surf. Sci. 20 (1985) 228.
[52] R. Vasquez, Surf. Sci. Spectra 1 (1992) 112.
[53] M. Machkova, N. Brashkova, P. Ivanov, J. Carda, V. Kozhukharov, Appl. Surf. Sci. 119 (1997) 127.
[54] R. Polini, A. Falsetti, E. Traversa, O. Schäf, P. Knauth, J. Eur. Ceram. Soc. 27 (2007) 4291.
[55] A.E. Bocquet, A. Fujimori, T. Mizokawa, T. Saitoh, H. Namatame, S. Suga, N. Kimizuka, Y. Takeda, M. Takano, Phys. Rev. B 45 (1992) 1561.
[56] R.J. Lad, V.E. Henrich, Surf. Sci. 193 (1988) 81.
[57] P. Mills, J. Sullivan, J. Phys. D: Appl. Phys. 16 (1983) 723.
[58] H. Yamashita, Y. Ichihashi, M. Takeuchi, S. Kishiguchi, M. Anpo, J. Synchrotron Radiat. 6 (1999) 451.
[59] A.E. Bocquet, A. Fujimori, T. Mizokawa, T. Saitoh, H. Namatame, S. Suga, N. Kimizuka, Y. Takeda, M. Takano, Phys. Rev. B 45 (1992) 1561.
[60] F. Amy, A. Wan, A. Kahn, F. Walker, R. Mckee, J. Appl. Phys. 96 (2004) 1635.
[61] D. Cahen, G. Hodes, M. Gratzel, J. Guillemoless, I. Riess, J. Phys. Chem. B 104 (2000) 2053.
[62] W.-J. Chun, A. Ishikawa, H. Fujisawa, T. Takata, J.N. Kondo, M. Hara, M. Kawai, Y. Matsumoto, K. Domen, J. Phys. Chem. B 107 (2003) 1798.
[63] G. Liu, W. Jaegermann, J. He, V. Sundström, L. Sun, J. Phys. Chem. B 106 (2002) 5814.
[64] J. Robertson, J. Vac. Sci. Technol., B 18 (2000) 1785.
[65] A. Rothschild, W. Menesklou, H.L. Tuller, E. Ivers-Tiffée, Chem. Mater. 18 (2006) 3651.
[66] A. Rothschild, S.J. Litzelman, H.L. Tuller, W. Menesklou, T. Schneider, E. Ivers-Tiffée, Sens. Actuators, B 108 (2005) 223.